ARTICLE

Band Alignment in WSe_2–Graphene Heterostructures

Kyounghwan Kim, Stefano Larentis, Babak Fallahazad, Kayoung Lee, Jiamin Xue, David C. Dillen, Chris M. Corbet, and Emanuel Tutuc*

Microelectronics Research Center, The University of Texas at Austin, Austin, Texas 78758, United States

ABSTRACT Using different types of WSe_2 and graphene-based heterostructures, we experimentally determine the offset between the graphene neutrality point and the WSe_2 conduction and valence band edges, as well as the WSe_2 dielectric constant along the *c*-axis. In a first heterostructure, consisting of WSe_2-on-graphene, we use the WSe_2 layer as the top dielectric in dual-gated graphene field-effect transistors to determine the WSe_2 capacitance as a function of thickness, and the WSe_2 dielectric constant along the *c*-axis. In a second heterostructure consisting of graphene-on-WSe_2, the lateral electron transport shows ambipolar behavior characteristic of graphene combined with a conductivity saturation at sufficiently high positive (negative) gate bias, associated with carrier population of the conduction (valence) band in WSe_2. By combining the experimental results from both heterostructures, we determine the band offset between the graphene charge neutrality point, and the WSe_2 conduction and valence band edges.

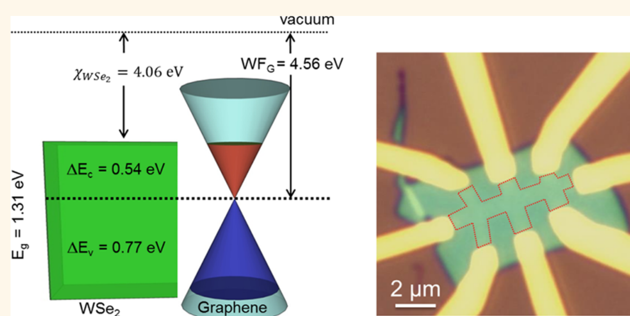

KEYWORDS: tungsten diselenide · graphene · heterostructure · band offset · band gap

Transition metal dichalcogenides (TMD)[1−3] possess interesting properties that render them attractive for electronic applications.[4] Similar to graphene, they have a two-dimensional (2D) character, can be isolated down to a monolayer, and have a relatively large bandgap (1−2 eV)[2] which helps overcome some of graphene's limitations for electronic and optoelectronic applications.[4,5] However, in order to assess and benchmark the potential of TMD materials and their heterostructures for applications, key fundamental properties such as carrier mobility, dielectric constant, and band offsets of different van der Waals heterostructures[6,7] need to be determined experimentally.

Tungsten diselenide (WSe_2) is a layered TMD semiconductor with a hexagonal crystal structure (a = 3.282 Å, c = 12.961 Å),[8] and band gap of ~1.2 eV[9,10] for bulk. Thanks to van-der-Waals bonding along the *c*-axis, WSe_2 can be mechanically exfoliated similarly to graphene. The WSe_2 band structure has been investigated theoretically,[11−13] and shown to undergo an indirect-to-direct gap transition in the monolayer limit,[12,14] a finding substantiated by photoluminescence measurements.[12,14,15] Several proof-of-concept devices, such as field-effect transistors (FETs),[16−18] solar cells,[19,20] light-emitting diode,[20,21] photodetector[22] and light-emitting transistors[23] have been demonstrated using WSe_2. However, a number of WSe_2 fundamental properties, such as intrinsic mobility, dielectric constant, and band alignment in heterostructures remain to be established.

RESULTS AND DISCUSSION

In this study, we experimentally investigate the electrical properties of WSe_2 using a combination of WSe_2 and graphene-based van der Waals heterostructures. Two different types of heterostructure are fabricated using a layer-by-layer transfer approach. A first heterostructure (HS #1) consists of WSe_2-on-graphene where we extract the WSe_2 dielectric constant (k_{WSe2}) along the *c*-axis thanks to a capacitance measurement as a function of WSe_2 thicknesses. In this structure, we use WSe_2 layer as the top dielectric of dual-gated graphene FETs. In a second heterostructure (HS #2) consisting of graphene-on-WSe_2, we observe ambipolar conduction in lateral transport, characteristic of graphene. At sufficiently high

* Address correspondence to etutuc@mer.utexas.edu.

Received for review February 17, 2015 and accepted March 13, 2015.

Published online March 13, 2015
10.1021/acsnano.5b01114

© 2015 American Chemical Society

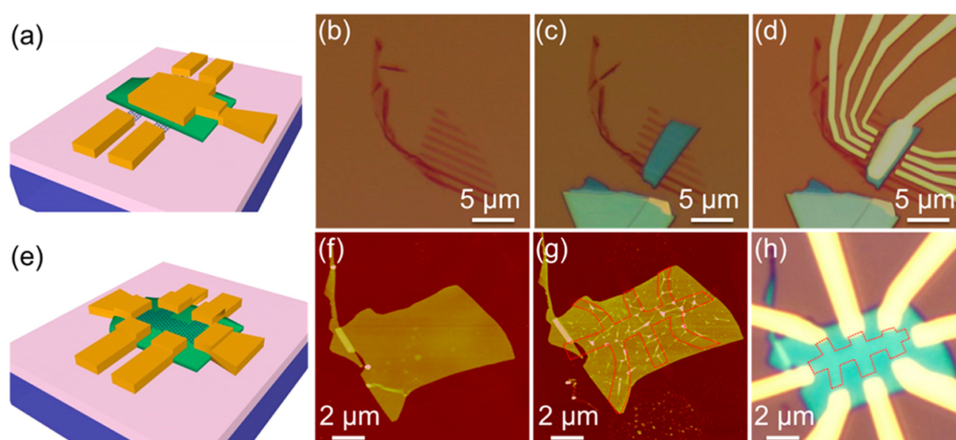

Figure 1. **(a) Schematic view of WSe_2-on-graphene heterostructure HS #1. (b) Optical micrograph of trimmed graphene on SiO_2, (c) WSe_2 layer transferred on graphene, and (d) completed device after metal deposition on WSe_2. (e) Schematic view of graphene-on-WSe_2 heterostructure (HS#2). (f) AFM topography of exfoliated WSe_2 after UHV anneal, and (g) transferred graphene on WSe_2. (h) Optical micrograph of completed device after Ni/Au deposition.**

positive (negative) gate bias, the conductivity saturates, a finding associated with carrier population of the conduction (valence) band in WSe_2. By combining the experimental results from the two types of heterostructures, we determine the energy offset between the graphene charge neutrality point and the WSe_2 conduction/valence band edges.

The fabrication processes of HS#1 and HS#2 is described in Figure 1a–d, and Figure 1e–h, respectively. The main difference between these two heterostructures is the stacking order of the graphene and WSe_2. The details of the fabrication process are described in the Materials and Methods section.

Figure 2 describes the electrical characteristics of HS #1 samples, where the top WSe_2 layer is used as a top dielectric in dual-gated graphene FETs. Figure 2a shows the graphene resistance (R) measured as a function of top-gate bias (V_{TG}), and at different fixed back gate biases (V_{BG}) ranging from −40 to 10 V. Each trace shows the typical ambipolar behavior of graphene FETs, with a neutrality point ($V_{TG,Dirac}$) which shifts as a function of V_{BG}. The linear dependence of $V_{TG,Dirac}$ *vs* V_{BG} data [Figure 2a inset] allows the extraction of the top WSe_2 capacitance (C_{TG}) using $\Delta V_{TG,Dirac}/\Delta V_{BG}$ = C_{BG}/C_{TG}; C_{BG} = 12.5 nF/cm^2 is the capacitance of 285 nm SiO_2, measured on separate metal pads. We note that since our analysis uses the gate bias values of the graphene charge neutrality, corresponding to zero chemical potential level, the graphene quantum capacitance does not play a role in this analysis.

To determine experimentally the value of k_{WSe2}, we examined the top-gate capacitance dependence on WSe_2 thickness (t_{WSe2}) on three devices with t_{WSe2} values of 4.6, 11.0, and 14.7 nm. Figure 2b shows the C_{TG}^{-1} as a function of t_{WSe2}. The t_{WSe2} values were determined by atomic force microscopy (AFM). Since the measurement accuracy of t_{WSe2} is important for this analysis, cross-sectional transmission electron microscopy

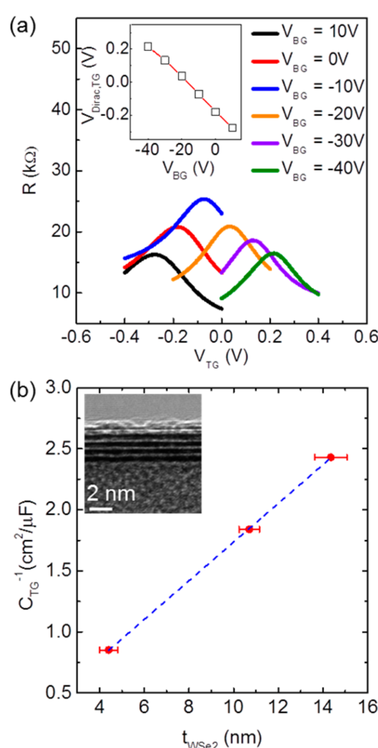

Figure 2. Electrical characteristics of HS #1 samples. (a) Resistance (R) *vs* V_{TG} of dual gated graphene FET, at V_{BG} ranging from −40 to 10 V. Inset: $V_{Dirac,TG}$ *vs* V_{BG}. (b) C_{TG}^{-1} *vs* t_{WSe2}. Inset: TEM cross section of exfoliated WSe_2 on SiO_2.

(TEM) of WSe_2 exfoliated on SiO_2 was used as a point of comparison for the AFM measurement of the WSe_2 thickness [Figure 2b inset]. On the basis of comparison between the AFM data with TEM cross-sectional result, we verified that the measured t_{WSe2} using AFM has an error of approximately one WSe_2 layer (∼0.7 nm), which is reflected in Figure 2b.

The top gate capacitance of HS#1 consists of two components, the WSe_2 capacitance in series with an interface capacitance (C_{int}). We can therefore write C_{TG} as

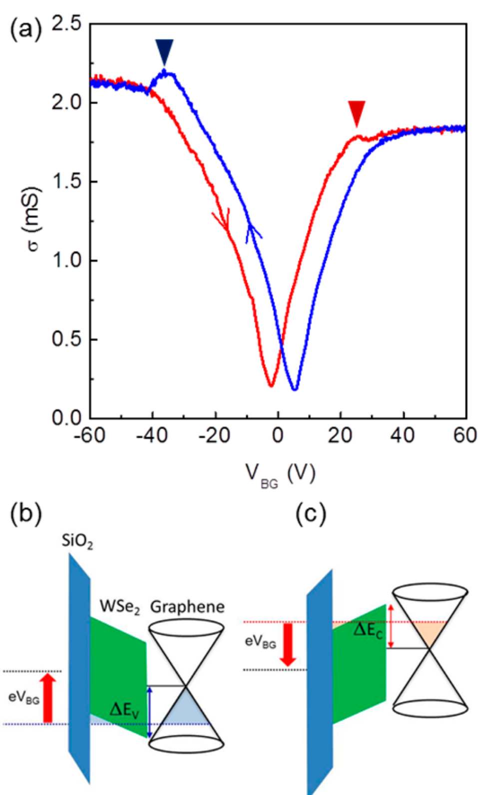

Figure 3. Electrical characteristics of HS#2 samples. (a) σ *vs* V_{BG} measured at T = 30 K for both V_{BG} sweep directions with 9.8 nm WSe_2 flake. At high positive (negative) gate bias the conductivity saturates, as marked in the figure, thanks to electrons (holes) populating the WSe_2. The finite hysteresis present when the WSe_2 is depleted of mobile carriers is associated with traps at the SiO_2−WSe_2 interface. (b and c) Band diagram across the heterostructure at high negative [panel b] and positive [panel c] gate bias illustrating the WSe_2 valence, and conduction band population, respectively.

$$C_{TG}^{-1} = C_{int}^{-1} + \frac{t_{WSe2}}{k_{WSe_2} \times \varepsilon_0} \quad (1)$$

where ε_0 is the vacuum dielectric permittivity. Using a linear fit to Figure 2b data, we extract $k_{WSe2} = 7.2 \pm 0.3$. This *k*-value will be later used in the following to determine the offset between the graphene charge neutrality point and band edges of WSe_2.

We now turn to the experimental investigation of HS #2 samples, consisting of graphene Hall bars on WSe_2 flakes. Figure 3a shows the four-point conductivity (σ) *vs* V_{BG} measured at a temperature T = 30 K, for a sample with t_{WSe2} = 9.8 nm. Figure 3a data are similar to the graphene ambipolar characteristics, except for a marked saturation at high positive and negative bias. The carrier mobility (μ) in graphene, extracted using $\mu = 1/C_{BG} \times d\sigma/dV_{BG}$ is 7000 $cm^2/V \cdot s$. Figure 3a also shows a finite hysteresis depending on the V_{BG} sweep direction. We address in the following both these findings.

At V_{BG} values below a certain threshold, marked in Figure 3a, the WSe_2 layer acts as a back-gate dielectric for graphene. While the back-gate induced electric field adds an electrostatic potential drop across the WSe_2, the chemical potential remains between the WSe_2 conduction and valence bands. At a positive (negative) V_{BG} threshold the electrostatic potential drop across the WSe_2 is sufficiently large to bring the WSe_2 conduction (valence) band edge at the WSe_2−SiO_2 interface in coincidence with the graphene chemical potential level [Figure 3b,c]. Once the WSe_2 starts to become populated with electrons (holes), the carrier density in graphene remains largely insensitive to V_{BG} as the WSe_2 carriers screen the back-gate, an observation which will be substantiated by Figure 4 data. The V_{BG} threshold depends on both the offset between the graphene neutrality point and the respective band edge, as well as on the WSe_2 thickness and dielectric constant. This observation is similar to experimental data in graphene−MoS_2 heterostructures,[24,25] where conductivity saturation corresponding to the MoS_2 becoming populated with electrons is observed at positive V_{BG} values. In graphene-on-WSe_2 heterostructures, however, we observe signatures of both the WSe_2 conduction and valence band becoming populated with carriers.

We attribute the hysteresis of σ *vs* V_{BG} of Figure 3a to a finite trap density at the WSe_2−SiO_2 interface. In a V_{BG} up-sweep (red trace) the traps become populated concomitantly with the population of the WSe_2 conduction band. During the V_{BG} back-sweep (blue trace), the delocalized electrons in the WSe_2 conduction band respond to the back-gate and are depleted, but the trap states remain charged down to the V_{BG} threshold corresponding to the WSe_2 valence band population with holes. Once the valence band becomes populated with holes, the delocalized holes render the traps charge neutral. This mechanism is confirmed by experimental data of graphene-on-WSe_2 heterostuctures using hexagonal boron nitride (hBN) as dielectric, where a negligible V_{BG} hysteresis is observed (see Supporting Information).

To further substantiate the mechanism described in Figure 3c,d, magnetotransport measurements were used to measure the carrier density in graphene as a function of V_{BG}. Figure 4a shows the longitudinal resistance (R_{xx}) of a graphene-on-WSe_2 heterostructure measured as a function of perpendicular magnetic field (B), at V_{BG} values ranging from −55 to 55 V. The data display Shubnikov-de Haas oscillations which we attribute to quantum Hall states (QHSs) in the graphene layer. The QHS filling factors $\nu = \pm 6$, 10, 14, 18 and 22, characteristic of monolayer graphene are marked on each trace. From Figure 4a data, we extract the graphene density (n_G) using $n_G = ((eB_\nu)/h)\nu$, where B_ν is the B-field value at filling factor ν, and e and h are electron charge and Plank constant, respectively. More specifically, at each V_{BG} value, we determine n_G using a linear fit to the B_ν vs $1/\nu \times (h/e)$ data. Figure 4b shows the n_G *vs* V_{BG} extracted from Figure 4a data for both the up-sweep and down-sweep V_{BG} directions. The data

show a linear n_G *vs* V_{BG} dependence at small V_{BG} values, expected for a back-gated graphene layer. At sufficiently large positive (negative) V_{BG} values, n_G departs from the linear dependence, and eventually saturates thanks to the WSe_2 becoming populated with electrons (holes).

To determine the band alignment in the graphene–WSe_2 heterostructure, it is instructive to examine the equilibrium conditions including the chemical potentials of the graphene (μ_G) and WSe_2 layer (μ_{WSe_2}). The graphene chemical potential density dependence is $\mu_G(n_G) = sgn(n_G)\hbar v_F(\pi|n_G|)^{1/2}$, where $v_F = 1.15 \times 10^8$ cm/s is the experimentally measured Fermi velocity;[26] the n_G values are positive (negative) for electrons (holes). If we reference μ_{WSe_2} with respect to the charge neutrality point of graphene, and define ΔE_C and ΔE_V as the offsets between the graphene neutrality point and the WSe_2 conduction and valence bands, respectively, it follows that $\mu_{WSe_2} = \Delta E_C$ when the WSe_2 chemical potential is at the conduction band edge, and $\mu_{WSe_2} = \Delta E_V$ when the WSe_2 chemical potential is at the valence band edge. The equilibrium condition between the graphene and WSe_2 writes:

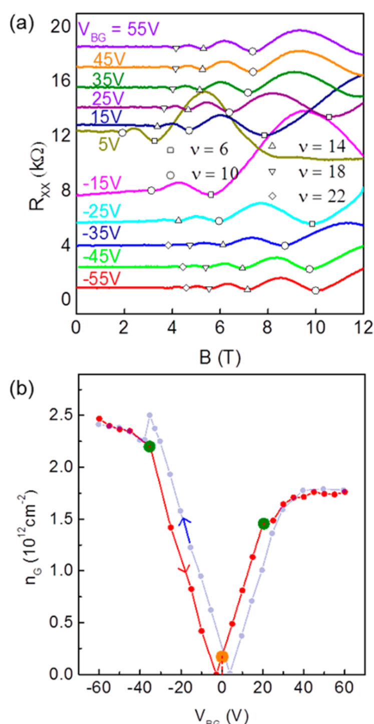

Figure 4. Magnetotransport properties of HS#2 samples. (a) R_{xx} *vs* B measured at different V_{BG} values and at T = 30 K. The SdH oscillations stem from QHSs in the graphene layer. The QHS filling factors ν are indicated in the figure. (b) n_G *vs* V_{BG} extracted panel a data.

$$\mu_G(n_G) + \frac{e^2 n_G}{\epsilon_{WSe2}\epsilon_0} t_{WSe_2} = \mu_{WSe_2} \qquad (2)$$

We note here that eq 2 is valid for a heterostructure where the graphene is assumed undoped at V_{BG} = 0 V. If the graphene has a finite doping density (n_0) at V_{BG} = 0 V stemming from residues or adsorbates on top of the graphene layer, eq 2 rewrites as

$$\mu_G(n_G) + \frac{e^2(n_G - n_0)}{\epsilon_{WSe2}\epsilon_0} t_{WSe_2} = \mu_{WSe_2} \qquad (3)$$

Therefore, by using the measured graphene carrier density at onset of the WSe_2 conduction (n_{GC}), and valence (n_{GV}) band population, along with n_0, the band offsets ΔE_C and ΔE_V band offset can be calculated as following:

$$\Delta E_C = \mu_G(n_{GC}) + \frac{e^2(n_{GC} - n_0)}{\epsilon_{WSe2}\epsilon_0} t_{WSe_2} \qquad (4)$$

$$\Delta E_V = \mu_G(n_{GV}) + \frac{e^2(n_{GV} - n_0)}{\epsilon_{WSe2}\epsilon_0} t_{WSe_2} \qquad (5)$$

The green symbols in Figure 4b mark the points at which the values of n_{GC} and n_{GV} are determined experimentally; the orange symbol marks the V_{BG} = 0 V point, where n_0 is extracted. Because of the finite hysteresis as a function of V_{BG}, for the purpose of calculating the band offsets, we use the V_{BG} up-sweep, during which the traps at the SiO_2–WSe_2 interface

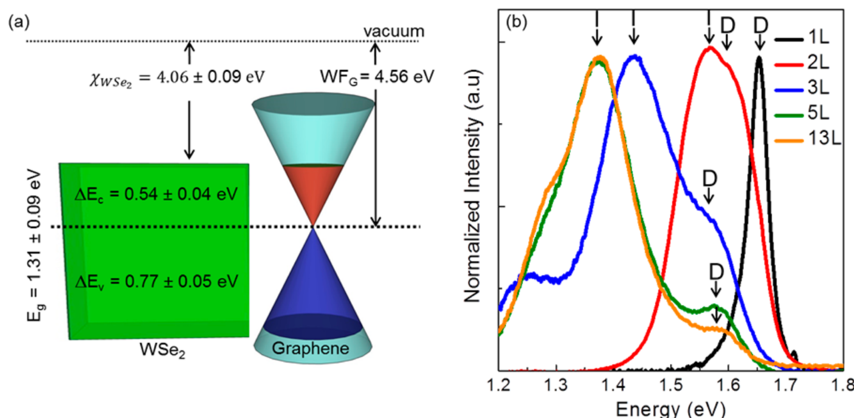

Figure 5. (a) Band alignment in the WSe_2–graphene heterostructure. (b) Normalized PL spectra of WSe_2 samples with various thicknesses. The data reveal two peaks, associated with the indirect (*I*) and direct (*D*) gap interband transitions.

remain unfilled up to WSe_2 conduction band population threshold.

Figure 5(a) summarizes the graphene-WSe_2 band alignment, including the electron affinity values. Using eqs 4 and 5, and experimental data from two samples with WSe_2 thickness of 9.8 nm (14 layers) and 10.5 nm (15 layers), respectively, we obtain $\Delta E_C = 0.54 \pm 0.04$ eV and $\Delta E_V = -0.77 \pm 0.05$ eV, and a corresponding WSe_2 bandgap of $E_G = \Delta E_C + |\Delta E_V| = 1.31 \pm 0.09$ eV. Using the graphene work function of 4.56 eV,[27,28] we calculate an electron affinity for WSe_2 of 4.06 ± 0.09 eV. Figure 5b shows photoluminescence (PL) measurement on WSe_2 flakes with different thicknesses, ranging from monolayer to more than 10 layers, measured at room temperature. The direct gap transition and indirect gap transitions are labeled as *D* and *I*, respectively. The indirect gap value determined from electrical characteristics of graphene-WSe_2 heterostructures is in good agreement with the PL measurement.

CONCLUSION

In summary, we introduced two types of heterostructures using graphene and WSe_2. By investigating their electrical characteristics we determine key heterostructure properties, such as WSe_2−graphene band alignment, and WSe_2 dielectric constant. These properties are instrumental in designing new device applications, such as graphene−WSe_2−graphene interlayer tunneling field-effect transistors similar to the graphene−hBN heterostructures.[29−32]

MATERIALS AND METHODS

Device Fabrication. For HS#1 samples, graphene is mechanically exfoliated on 285 nm thick SiO_2/Si substrates. Raman spectroscopy and optical contrast are used to identify the monolayer flakes. Electron beam lithography (EBL) and O_2 plasma etching are used to define a set of 1−2 μm-wide stripes [Figure 1b], followed by ultrahigh-vacuum (UHV) anneal at 350 °C to remove the resist residues. WSe_2 flakes, exfoliated onto separate substrates, are then aligned and transferred onto the graphene layer [Figure 1c] using a mask aligner with a heated sample holder.[33] After transfer, the samples are annealed again in UHV at 350 °C. A second EBL followed by metal (Ni/Au) deposition is used to define contacts to the graphene layer, as well as a top-gate onto the WSe_2 flake [Figure 1d].

The fabrication of HS#2 is similar, but the opposite order of stacking is used. WSe_2 flakes are first mechanically exfoliated on 285 nm SiO_2/Si substrates, followed by 350 °C UHV annealing to remove tape residue. The flake thickness and topography were probed by atomic force microscopy (AFM) [Figure 1e]. Monolayer graphene flakes, exfoliated onto separate substrates, are aligned and transferred onto the WSe_2 [Figure 1f]. After transfer, EBL and O_2 plasma etching are used to define a Hall bar shape on the graphene monolayer [Figure 1e], followed by a second UHV anneal at 350 °C to remove the resist residues. A second EBL and metal (Ni/Au) deposition are used to define contacts to the graphene layer [Figure 1g].

Electrical Characterization. The electrical characterization is done using a combination of DC and small signal lock-in measurements, in a variable temperature refrigerator with a base temperature (T) of $T = 1.5$ K, and in magnetic fields up to 12 T.

Conflict of Interest: The authors declare no competing financial interest.

Acknowledgment. This was supported in part by the NRI, Intel Corp., and National Science Foundation grant DMR-0846573.

Supporting Information Available: Conductivity *vs* back-gate bias dependence in graphene-on-WSe2 heterostructures on SiO_2 and hBN substrates. This material is available free of charge *via* the Internet at http://pubs.acs.org.

REFERENCES AND NOTES

1. Novoselov, K. S.; Jiang, D.; Schedin, F.; Booth, T. J.; Khotkevich, V. V.; Morozov, S. V.; Geim, A. K. Two-Dimensional Atomic Crystals. *Proc. Natl. Acad. Sci. U.S.A.* **2005**, *102*, 10451–10453.
2. Wang, Q. H.; Kalantar-Zadeh, K.; Kis, A.; Coleman, J. N.; Strano, M. S. Electronics and Optoelectronics of Two-Dimensional Transition Metal Dichalcogenides. *Nat. Nanotechnol.* **2012**, *7*, 699–712.
3. Chhowalla, M.; Shin, H. S.; Eda, G.; Li, L. J.; Loh, K. P.; Zhang, H. The Chemistry of Two-Dimensional Layered Transition Metal Dichalcogenide Nanosheets. *Nat. Chem.* **2013**, *5*, 263–275.
4. Jariwala, D.; Sangwan, V. K.; Lauhon, L. J.; Marks, T. J.; Hersam, M. C. Emerging Device Applications for Semiconducting Two-Dimensional Transition Metal Dichalcogenides. *ACS Nano* **2014**, *8*, 1102–1120.
5. Lopez-Sanchez, O.; Lembke, D.; Kayci, M.; Radenovic, A.; Kis, A. Ultrasensitive Photodetectors Based on Monolayer MoS_2. *Nat. Nanotechnol.* **2013**, *8*, 497–501.
6. Geim, A. K.; Grigorieva, I. V. Van der Waals Heterostructures. *Nature* **2013**, *499*, 419–425.
7. Liu, X. Z.; Galfsky, T.; Sun, Z.; Xia, F. N.; Lin, E. C.; Lee, Y. H.; Kena-Cohen, S.; Menon, V. M. Strong Light-Matter Coupling in Two-Dimensional Atomic Crystals. *Nat. Photonics* **2015**, *9*, 30–34.
8. Schutte, W. J.; Deboer, J. L.; Jellinek, F. Crystal-Structures of Tungsten Disulfide and Diselenide. *J. Solid State Chem.* **1987**, *70*, 207–209.
9. Upadhyay, Lc; Loferski, J. J.; Wold, A.; Giriat, W.; Kershaw, R. Semiconducting Properties of Single Crystals of N and P-Type Tungsten Diselenide (Wse_2). *J. Appl. Phys.* **1968**, *39*, 4736.
10. Yousefi, G. H. Optical-Properties of Mixed Transition-Metal Dichalcogenide Crystals. *Mater. Lett.* **1989**, *9*, 38–40.
11. Jiang, H. Electronic Band Structures of Molybdenum and Tungsten Dichalcogenides by the GW Approach. *J. Phys. Chem. C* **2012**, *116*, 7664–7671.
12. Zeng, H. L.; Liu, G. B.; Dai, J. F.; Yan, Y. J.; Zhu, B. R.; He, R. C.; Xie, L.; Xu, S. J.; Chen, X. H.; Yao, W.; et al. Optical Signature of Symmetry Variations and Spin-Valley Coupling in Atomically Thin Tungsten Dichalcogenides. *Sci. Rep.* **2013**, *3*, 1608.
13. Wickramaratne, D.; Zahid, F.; Lake, R. K. Electronic and Thermoelectric Properties of Few-Layer Transition Metal Dichalcogenides. *J. Chem. Phys.* **2014**, 140.
14. Zhao, W. J.; Ribeiro, R. M.; Toh, M. L.; Carvalho, A.; Kloc, C.; Neto, A. H. C.; Eda, G. Origin of Indirect Optical Transitions in Few-Layer MoS_2, WS_2, and WSe_2. *Nano Lett.*. **2013**, *13*, 5627–5634.
15. Tonndorf, P.; Schmidt, R.; Bottger, P.; Zhang, X.; Borner, J.; Liebig, A.; Albrecht, M.; Kloc, C.; Gordan, O.; Zahn, D. R. T.; et al. Photoluminescence Emission and Raman Response of Monolayer MoS_2, $MoSe_2$, and WSe_2. *Opt. Express* **2013**, *21*, 4908–4916.
16. Podzorov, V.; Gershenson, M. E.; Kloc, C.; Zeis, R.; Bucher, E. High-Mobility Field-Effect Transistors Based on Transition Metal Dichalcogenides. *Appl. Phys. Lett.* **2004**, *84*, 3301–3303.

17. Fang, H.; Chuang, S.; Chang, T. C.; Takei, K.; Takahashi, T.; Javey, A. High-Performance Single Layered WSe_2 p-FETs with Chemically Doped Contacts. *Nano Lett.* **2012**, *12*, 3788–3792.
18. Liu, W.; Kang, J. H.; Sarkar, D.; Khatami, Y.; Jena, D.; Banerjee, K. Role of Metal Contacts in Designing High-Performance Monolayer n-Type WSe_2 Field Effect Transistors. *Nano Lett.* **2013**, *13*, 1983–1990.
19. Prasad, G.; Srivastava, O. N. The High-Efficiency (17.1-Percent) Wse_2 Photo-Electrochemical Solar-Cell. *J. Phys. D: Appl. Phys.* **1988**, *21*, 1028–1030.
20. Pospischil, A.; Furchi, M. M.; Mueller, T. Solar-Energy Conversion and Light Emission in an Atomic Monolayer p-n Diode. *Nat. Nanotechnol.* **2014**, *9*, 257–261.
21. Ross, J. S.; Klement, P.; Jones, A. M.; Ghimire, N. J.; Yan, J. Q.; Mandrus, D. G.; Taniguchi, T.; Watanabe, K.; Kitamura, K.; Yao, W.; et al. Electrically Tunable Excitonic Light-Emitting Diodes Based on Monolayer WSe_2 p-n Junctions. *Nat. Nanotechnol.* **2014**, *9*, 268–272.
22. Baugher, B. W. H.; Churchill, H. O. H.; Yang, Y. F.; Jarillo-Herrero, P. Optoelectronic Devices Based on Electrically Tunable p-n Diodes in a Monolayer Dichalcogenide. *Nat. Nanotechnol.* **2014**, *9*, 262–267.
23. Zhang, Y. J.; Oka, T.; Suzuki, R.; Ye, J. T.; Iwasa, Y. Electrically Switchable Chiral Light-Emitting Transistor. *Science* **2014**, *344*, 725–728.
24. Larentis, S.; Tolsma, J. R.; Fallahazad, B.; Dillen, D. C.; Kim, K.; MacDonald, A. H.; Tutuc, E. Band Offset and Negative Compressibility in Graphene-MoS_2 Heterostructures. *Nano Lett.* **2014**, *14*, 2039–2045.
25. Yankowitz, M.; Larentis, S.; Kim, K.; Xue, J.; McKenzie, D.; Huang, S.; Paggen, M.; Ali, M. N.; Cava, R. J.; Tutuc, E.; LeRoy, B. J. Intrinsic Disorder in Graphene on Transition Metal Dichalcogenide Heterostructures. *Nano Lett.* **2015**, *15*, 1925–1929.
26. Kim, S.; Jo, I.; Dillen, D. C.; Ferrer, D. A.; Fallahazad, B.; Yao, Z.; Banerjee, S. K.; Tutuc, E. Direct Measurement of the Fermi Energy in Graphene Using a Double-Layer Heterostructure. *Phys. Rev. Lett.* **2012**, 108.
27. Yan, R. S.; Zhang, Q.; Li, W.; Calizo, I.; Shen, T.; Richter, C. A.; Hight-Walker, A. R.; Liang, X. L.; Seabaugh, A.; Jena, D.; et al. Determination of Graphene Work Function and Graphene-Insulator-Semiconductor Band Alignment by Internal Photoemission Spectroscopy. *Appl. Phys. Lett.* **2012**, 101.
28. Yu, Y. J.; Zhao, Y.; Ryu, S.; Brus, L. E.; Kim, K. S.; Kim, P. Tuning the Graphene Work Function by Electric Field Effect. *Nano Lett.* **2009**, *9*, 3430–3434.
29. Britnell, L.; Gorbachev, R. V.; Jalil, R.; Belle, B. D.; Schedin, F.; Mishchenko, A.; Georgiou, T.; Katsnelson, M. I.; Eaves, L.; Morozov, S. V.; et al. Field-Effect Tunneling Transistor Based on Vertical Graphene Heterostructures. *Science* **2012**, *335*, 947–950.
30. Georgiou, T.; Jalil, R.; Belle, B. D.; Britnell, L.; Gorbachev, R. V.; Morozov, S. V.; Kim, Y. J.; Gholinia, A.; Haigh, S. J.; Makarovsky, O.; et al. Vertical Field-Effect Transistor Based on Graphene-WS_2 Heterostructures for Flexible and Transparent Electronics. *Nat. Nanotechnol.* **2013**, *8*, 100–103.
31. Fallahazad, B.; Lee, K.; Kang, S.; Xue, J. M.; Larentis, S.; Corbet, C.; Kim, K.; Movva, H. C. P.; Taniguchi, T.; Watanabe, K.; et al. Gate-Tunable Resonant Tunneling in Double Bilayer Graphene Heterostructures. *Nano Lett.* **2015**, *15*, 428–433.
32. Kang, S.; Fallahazad, B.; Lee, K.; Movva, H.; Kim, K.; Corbet, C.; Taniguchi, T.; Watanabe, K.; Colombo, L.; Register, L.; et al. Bilayer Graphene-Hexagonal Boron Nitride Heterostructure Negative Differential Resistance Interlayer Tunnel FETs. *IEEE Electron Device Lett.* **2015**, 10.1109/LED.2015.2398737.
33. Dean, C. R.; Young, A. F.; Meric, I.; Lee, C.; Wang, L.; Sorgenfrei, S.; Watanabe, K.; Taniguchi, T.; Kim, P.; Shepard, K. L.; et al. Boron Nitride Substrates for High-Quality Graphene Electronics. *Nat. Nanotechnol.* **2010**, *5*, 722–726.